A Robust Anti-Thermal-Quenching Phosphor Based on Zero-Dimensional Metal Halide Rb3InCl6:xSb3+

Journal:	*Journal of the American Chemical Society*
Manuscript ID	ja-2023-14137t.R2
Manuscript Type:	Article
Date Submitted by the Author:	18-Feb-2024
Complete List of Authors:	Zhang, Baowei; Zhengzhou University Ru, Yi; Zhengzhou University Zhou, Jiaqian; Zhengzhou University Jia, Jingtao; Zhengzhou University Song, Haoqiang; Zhengzhou University Liu, Zhongyi; Zhengzhou Univetsity, Zhang, Linlin; School of Materials Science and Engineering, Zhengzhou University, Liu, Xuying; Zhengzhou University, School of Materials Science and Engineering Zhong, Gui-Ming; 21C Innovation Laboratory, Contemporary Amperex Technology Ltd. (21C LAB) Yong, Xue; University of Liverpool, Department of Electrical Engineering and Electronics Panneerselvam, Iyyappa Rajan; Istituto Italiano di Tecnologia Manna, Liberato; Istituto Italiano di Tecnologia, ; Lu, Siyu; Zhengzhou University,

A Robust Anti-Thermal-Quenching Phosphor Based on Zero-Dimensional Metal Halide Rb_3InCl_6:xSb^{3+}

Baowei Zhang,[a,▽] Yi Ru,[a,▽] Jiaqian Zhou,[a] Jingtao Jia,[a] Haoqiang Song,[a] Zhongyi Liu,[a] Linlin Zhang,[b] Xuying Liu,[b] Gui-Ming Zhong,[c] Xue Yong,[d] Iyyappa Rajan Panneerselvam,[e] Liberato Manna,[e,*] Siyu Lu[a,*]

[a] College of Chemistry, Zhengzhou University, Zhengzhou 450000, China.

[b] School of Materials Science and Engineering, Zhengzhou University, Zhengzhou, 450001 P. R. China.

[c] 21C Innovation Laboratory, Contemporary Amperex Technology Ltd. (21C LAB), Ningde, 352100 China.

[d] Department of Electrical Engineering and Electronics, University of Liverpool, Liverpool, L69 3GJ, U.K.

[e] Nanochemistry, Istituto Italiano di Tecnologia, via Morego 30, 16163 Genova, Italy.

KEYWORDS. Anti-Thermal Quenching; Metal Halide Perovskites; High-Power White Light Emitting Diodes;

Abstract: High-power phosphor-converted white light emitting diodes (hp-WLEDs) have been widely involved in modern society as outdoor lighting sources. In these devices, due to the Joule effect, the high applied currents cause high operation temperatures (> 500 K). Under these conditions, most phosphors lose their emission, an effect known as thermal quenching (TQ). Here, we introduce a zero-dimensional (0D) metal halide, Rb_3InCl_6:xSb^{3+}, as a suitable anti-TQ phosphor offering robust anti-TQ behavior up to 500 K. We ascribe this behavior of the metal halide to two factors: (1) a compensation process via thermally-activated energy transfer from structural defects to emissive centers; and (2) an intrinsic structural rigidity of the isolated octahedra in the 0D structure. The anti-TQ phosphor based WLEDs can stably work at a current of 2000 mA. The low synthesis cost, non-toxic composition reported here can herald a new generation of anti-TQ phosphors for hp-WLED.

Introduction

Outdoor lighting plays a pivotal role in night-time human activities and accounts for ~40% electricity consumption in urban cities.[1] High-power phosphor-converted white light-emitting diodes (hp-WLEDs) have been widely employed for outdoor lighting, thanks to their ~10× efficiency compared to traditional lighting, which significantly reduces energy consumption, hence greenhouse gas emissions.[2] High power means high applied work currents (>200 mA), which entail high operating temperatures for hp-WLEDs (up to over 500 K)[3] due to the Joule heating effect. Such high temperatures activate non-radiative relaxation channels of the phosphor and thus result in emission efficiency losses, an effect known as thermal quenching (TQ).[4,5] To reduce TQ, an ideal candidate phosphor for hp-WLED should minimize its thermally-activated non-radiative processes while compensating the emission losses at increasing temperature.[2,6-9] The first feature requires a high structural rigidity of the phosphor,[9,10] whereas the second feature requires an energy transfer process from traps (or other sensitizers) to luminescence centers.[7,9,11,12] Metal oxide/nitrides doped with rare earths or transition metals are the mainstream materials for anti-TQ phosphors[2,9,13,14] and are widely applied in hp-WLED.[6,15-17] For example, Kim et.al reported zero TQ up to 473 K from a blue-emitting $Na_{3-2x}Sc_2(PO_4)_3$:xEu^{2+} phosphor,[2] its thermally-stable emission being ascribed to a compensation process via a thermally-activated energy transfer from structural defects to Eu^{2+} emitting centers.[2] With that phosphor they fabricated a hp-WLED that could work stably at high currents, up to 1000 mA. Subsequently, Qiao et.al doped Eu^{2+} into a rigid $K_2BaCa(PO_4)_2$ structure to obtain an anti-TQ phosphor. Thanks to the well-designed rigid structure,[18] the $K_2BaCa(PO_4)_2$:xEu^{2+} phosphor exhibited stable or even enhanced luminescence with increasing temperature, up to 548 K.[9] Ma et.al proposed a self-defect engineering approach for $Li_2Sr_{1-x-\Delta}SiO_4$:x% Eu^{2+} ($0.2 \le x \le 3.0$, $0.1\% \le \Delta \le 5\%$), where the stoichiometric (Δ) deficiency of the Sr precursor was meant to induce the formation of intrinsic defects. Via efficient energy transfer from defects to Eu^{2+} emitting centers, in the optimal sample (Δ = 0.1%) the PL intensity at 498 K corresponded to 114% of its initial value at room temperature.[19]

The problem with metal oxides/nitrides is that their syntheses require high temperatures (>1500 K).[7] Metal halides, on the other hand, can profit from the much lower synthesis temperatures (some of them can be even prepared at room temperature) and, for some members of the class, high photoluminescence quantum yield (PLQY). Indeed, various metal halides have been explored as potential candidates for anti-TQ phosphors.[10-12,20] Several Sb doped metal halides were reported to have good thermal stability of their luminescence, although far lower than any other reported metal oxide/nitride based anti-TQ phosphor.[21,22] Huang et.al reported Mn^{2+} doped $CsPb(Cl/Br)_3$ halide perovskite nanocrystals offering thermally stable (or even enhanced) red emission up to 323 K, which was attributed to thermally activated energy transfer from excitonic to Mn^{2+} acceptor states.[11,23] Liu et.al reported fluorine treated $CsPbBr_3$ perovskite nanocrystals with a temperature-independent emission from 298 K to 373 K.[10] The fluorine rich shell was purported to have a wider energy gap than the inner nanocrystal core, suppressing carrier trapping and improving thermal stability.[8,10] Han et.al found that a Mn^{2+} doped $Rb_3Cd_2Cl_7$

single crystals did not suffer from luminescence intensity quenching up to 423 K.[20,24,25] More recently, Zhou et.al developed a Zr^{4+}/Mn^{2+} co-doped $CsCdCl_3$ system featuring a robust anti-TQ radioluminescence up to 448 K, a record value for metal halides materials.[12] The authors hypothesized that the thermally stable radioluminescence was due to compensation of the emission losses at high temperatures by a thermally activated energy transfer from defects to the Mn^{2+} emitters. By co-doping with Zr^{4+}, the trap depth and distribution were further modulated. Hence, the better anti-TQ behavior was rationalized as due to traps at progressively higher depth and broader distribution that could compensate the emission losses at higher temperatures.[12] Yet, even though anti-TQ metal halide perovskite phosphors have been intensely explored in the last three years, their anti-TQ behavior still lags behind that of the metal nitride/oxide-based phosphors.[10-12,20] More importantly, they are either Pb-based[10,11] or Cd-based hosts,[12,20,25,26] which are toxic.

Here we report a non-toxic and rare-earth-free metal halide phosphor, $Rb_3InCl_6:xSb^{3+}$ (x = ~1%), in the form of a powder sample (synthesized at 483 K in an autoclave), exhibiting robust anti-TQ behavior. This material has a zero-dimensional (0D) phase formed by isolated $[InCl_6]^{3-}$ octahedra (with a small fraction of the In^{3+} ions replaced by Sb^{3+} ones) that are charge balanced by A^+ cations, and show green emission with ~90% PLQY.[27-29] In the synthesis, the In precursor was added in a sub-stoichiometric amount, that is $(1-\Delta)\cdot n_{moles}$ (where n_{moles} would correspond to the stoichiometric amount required to synthesize Rb_3InCl_6) with the aim to induce the formation of structural defects.[19] By tuning the stoichiometric deficiency Δ (henceforth reported in % terms, that is, Δ/100) of the added In precursors and alloying at the Rb site with other cations (K, Cs), we could prepare optimal $Rb_{3-y}Cs_yInCl_6:xSb^{3+}$ samples that did not show luminescence quenching at temperatures up to 500 K, making them comparable to the best metal oxide/nitride based anti-TQ phosphors to date.[2,7,9] The sample's structure and luminescence were preserved after several cycles of heating-cooling. To shed light onto the key factors determining the anti-TQ behavior, a series of control experiments was carried out. We determined that by adjusting the stoichiometric deficiency Δ of the In precursors we could modulate the depth and distribution of the energy traps. Specifically, by thermoluminescence (TL) spectroscopy we could assess that, with increasing temperature, in $A_3InCl_6:xSb^{3+}$ the high density of traps could compensate the emission losses of self-trapped exciton emission (STE) by thermally activated energy transfer.[12]

By temperature-dependent X-ray diffraction (XRD) we could prove that alloying at the A site can be exploited to adjust the structural rigidity of $A_3InCl_6:xSb^{3+}$. In detail, partial alloying of the Rb^+ ions with the larger Cs^+ ions entailed a higher structural rigidity, as revealed by the smaller expansion of the cell compared to the non-alloyed one at increasing temperature. In contrast, partial alloying of the Rb^+ ions with the smaller K^+ ions led to a larger expansion of the cell at increasing temperature. A higher structural rigidity of the Cs-Rb alloyed sample is the most likely cause of the more efficient suppression of the thermally activated non-radiative processes, leading to a better anti-TQ behavior.[7,30] As a comparison, we also synthesized powders of a three-dimensional (3D) $Cs_2AgInCl_6:xSb^{3+}$ double perovskite sample, which instead did not show any obvious anti-TQ behavior. By Rietveld refinement of the XRD patterns and Raman analysis we could verify that, with increasing temperature, the isolated octahedra in 0D $Rb_3InCl_6:xSb^{3+}$ expanded less (in terms of metal-halide bond length) than the whole unit cell, indicating that what mostly changed was the inter-octahedra distance in this case. By contrast, the connected octahedra in 3D $Cs_2AgInCl_6:xSb^{3+}$ followed a linear expansion that matched the expansion of the whole unit cell. In this context, we attribute the structural rigidity of the 0D $Rb_3InCl_6:xSb^{3+}$ structure to the low dependence on temperature of the expansion/distortion of the isolated octahedra, which are indeed the emitting centers.

These powders were then employed in a hp-WLED device that demonstrated stable lighting intensity and color coordinates even under a current of 2000 mA, corresponding to an operating temperature of ~500 K. The non-toxic and rare-earth metal free 0D metal halides materials reported here, thanks to their simple and scalable synthesis, represent a new generation of anti-TQ phosphors for hp-WLED devices.

Results and Discussion

Synthesis and anti-TQ emission. The $Rb_3InCl_6:xSb^{3+}$ samples were synthesized by grinding together RbCl, $InCl_3$, and $SbCl_3$ powders. The number of moles of $InCl_3$ added corresponded to 3*(1-Δ) mmol, slightly lower than the 3 mmol amount required for a stoichiometric synthesis. The ground powders were mixed with methanol in an autoclave which was then heated at 210 °C for 22 hours. After that, the solution was dried in an oven. The final sample was a white powder showing a bright green emission (under 365 nm UV lamp) peaked at 521 nm, with a PLQY over 90% (Figure S1), consistent with previous reports.[27-29] The synthesized Sb doped Rb_3InCl_6 have a monoclinic phase, as assessed by XRD analysis. For comparison, the Sb doped Rb_3InCl_6 sample synthesized with a stoichiometric amount of $InCl_3$ (named as reference sample) was also prepared.[27]

We then recorded the photoluminescence (PL) spectra of the prepared sample as a function of temperature in the 300-500 K range (Fig. 1a, b and c). We refer here to the $Rb_3InCl_6:xSb^{3+}$ sample prepared with Δ = 1.1% and 1.3% Sb. With increasing temperature, the PL spectra of the $Rb_3InCl_6:xSb^{3+}$ sample slight blue-shifted (Figure 1a), while its PL intensity (Figure 1b) evidenced a gentle upward trend up to a maximum at around 400 K (corresponding to ~125% of the initial value at room temperature RT) and then slowly decreased, preserving essentially 100% of its initial (RT) value at 450 K. In contrast, the PL intensity of the reference sample followed immediately a downward trend, retaining only ~35% of its initial RT value at 450 K (Figure S2 and Figure 1b).

The $Rb_3InCl_6:xSb^{3+}$ sample was then subjected to multiple cycles of heating-cooling from 300 K to 400 K and back, with the corresponding PL intensity being measured at each turning point (Figure 1c and Figure S3). No significant loss of PL intensity was observed after many cycles, pointing to a robust anti-TQ behavior. We also recorded XRD patterns

at various temperatures during a heating cooling cycle (Figures 1d and S4) from 298 K to 523 K and back, by which we could verify that the sample remained structurally stable. In details, the diffraction peaks gradually shifted to lower (higher) 2ϴ angles with increasing (decreasing) temperature, and returned to their initial position when cooling back to RT, without generating any impurity peaks.[2,31] Hence, the sample underwent a reversible lattice expansion-contraction with a slope of $-1.9*10^{-3}$ $2\theta/K^{-1}$ (Figure S4 and Figure 1d). Overall, we can state that the $Rb_3InCl_6:xSb^{3+}$ sample exhibited robust, both reversible luminescence stability and structural stability upon heating/cooling. Based on the well-studied metal oxide/nitride system, we assume that both defects and structural rigidity can play a key role in compensating the thermally activated emission losses.[7,11,12] A series of control experiments were then carried out to study the key parameters regulating the anti-TQ properties of $Rb_3InCl_6:xSb^{3+}$. They are described in the following sections.

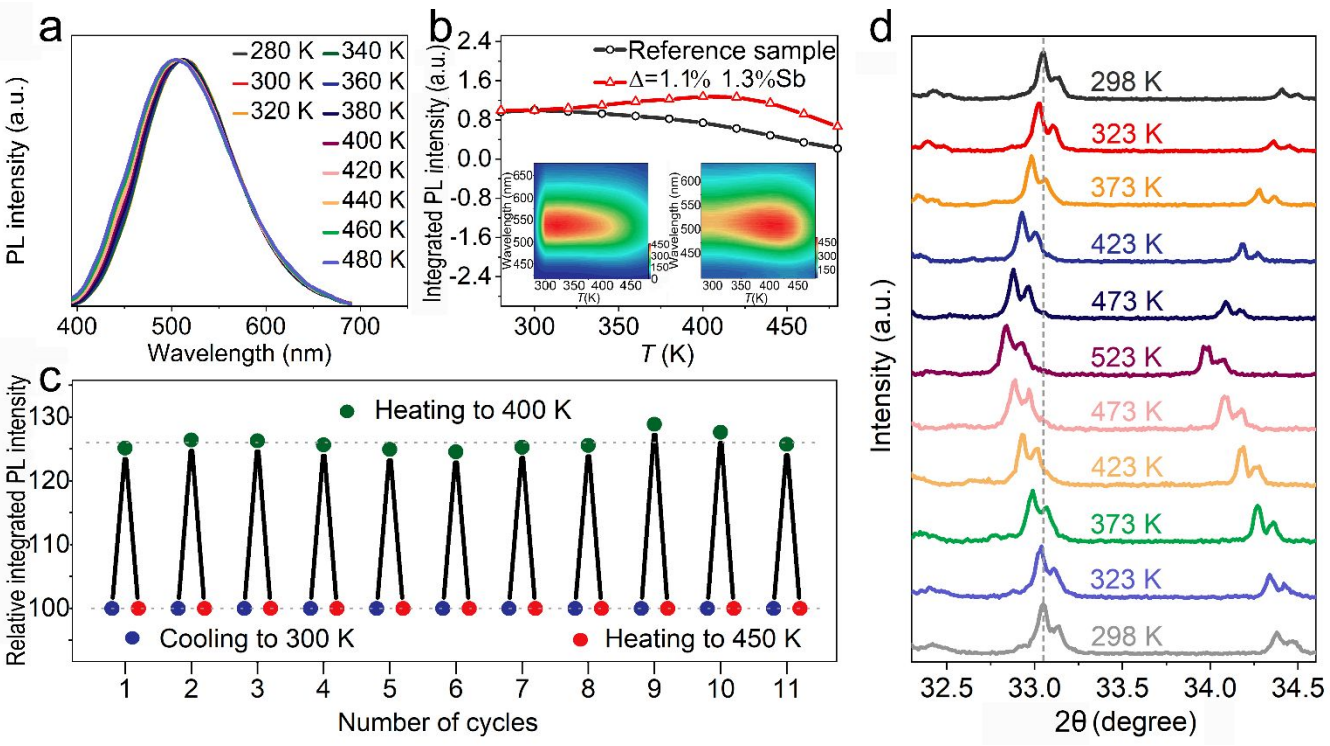

Figure 1. (a) PL spectra of a $Rb_3InCl_6:xSb^{3+}$ (Δ = 1.1% and x = 1.3%) powder sample as a function of temperature from 280 K to 480 K (excitation at 375 nm). (b) Temperature-dependent PL intensity of the sample (Δ = 1.1% and x = 1.3%) and the reference $Rb_3InCl_6:xSb^{3+}$ sample (Δ = 0%) when heated from 300 to 500 K, normalized by referencing the initial PL intensity at 300 K as 1. (c) Stability test, consisting of 11 cycles of heating-cooling. In each cycle the PL intensity is measured at 300 K (blue dots), 400 K (green dots) and 450 K (red dots). The PL intensity values are normalized to the starting value of each cycle recorded at 300 K. (d) XRD spectra of $Rb_3InCl_6:xSb^{3+}$ during a heating-cooling cycle, this time in the temperature range from 298 K to 523 K.

Mechanism and control experiments. The Sb doping amount was optimized to a value of 1.3%, as this value was found to yield the highest values of PLQY and the best anti-TQ behavior, as shown in Figure S5-8 and Tables S2-4. Hence, we fixed the Sb doping amount in the range of 1%-2% in the following study. We then synthesized different samples at various stoichiometric deficiencies (Δ) of the $InCl_3$ precursors. The whole series comprises 1.1%, 1.3%, 1.5%, 1.7%, 1.9% (corresponding to 2.967 mmol, 2.961 mmol, 2.955 mmol, 2.949 mmol and 2.943 mmol $InCl_3$, respectively, Table S1). By elemental analysis via inductively coupled plasma optical emission spectroscopy (ICP-OES) and scanning electron microscopy energy dispersive spectroscopy (SEM-EDS), the Sb amount (x) was determined to be in the 1%-1.4% range (Figure S9-S14, Table S5-9). We then recorded the temperature dependent PL spectra for each sample (Figure 2a and Figure S15). To help with the discussion, we define the critical temperature (T_c) as the one at which the PL intensity was equal to 100% of the initial PL intensity at 300 K. We then used T_c to evaluate the anti-TQ properties of each sample. As shown in Figure 2a, T_c initially increased with increasing Δ and reached a maximum value of 491 K for Δ = 1.5%. The Δ = 1.5% sample showed reproducible luminesce stability under cycles of heating-cooling (Figure S16) and also evidenced long-term luminesce stability upon heating (Figure S17).

Elemental analyses such as ICP-OES and SEM-EDS could not distinguish the tiny differences in In stoichiometry across the samples prepared at various Δ. Yet, the XRD patterns of the same samples evidenced a slight but steady shift to higher angles with increasing Δ (Figure 2b). This can be explained by assuming that at higher Δ the samples have a higher density of structural vacancies, resulting in slight contraction of the lattice.[19] The formation of vacancies was further proven by ^{85}Rb magic angle spinning (MAS) nuclear magnetic resonance (NMR) characterization (Figure S18),

which evidenced at least four different ^{85}Rb peaks in the range from 100 to -100 ppm. Considering that Rb^+ ions occupy two different locations (Rb_1, Rb_2) in the tetragonal Rb_3InCl_6 phase,[22] the NMR spectra indicated that the two types Rb atom could be surrounded by either 6 $[InCl_6]^{3-}$ or 5 $[InCl_6]^{3-}$ octahedra and 1 In vacancy,[32,33] which further splits the number of Rb sites to four, (Rb_1, Rb_{1-v}) and (Rb_2, Rb_{2-v}), resulting in 2*2 multiplets. As the synthesis conditions employ non-stoichiometric ratios (in particular, insufficient In precursors), the defects here could be B^{3+} site vacancies, with an energy depth of 0.8-1.0 eV and a density of $2.3*10^{10}$ cm^{-3}, as determined by thermally stimulated current (TSC) and space-charge-limited current (SCLC) analyses (reported in Figure S19).

We then tried to rationalize the role played by the vacancies on the energy traps by recording thermoluminescence (TL) spectra (Figures 2c). The trap depth (E_T) was estimated empirically by $E_T = T_m/500$ eV, where T_m is the temperature at which the TL curve reaches a maximum.[34] In details, the trap types could be divided into three regions, according to trap depth: type I (300-400 K, E_T=0.7 eV), type II (400-550 K, E_T=1.0 eV) and type III (>550 K, E_T=1.2 eV), as shown in Figure 2c. The trap depth gradually increased by increasing Δ and their distribution reached maximum broadening at Δ = 1.5%. Further increase in Δ resulted in a narrower energy distribution along with the disappearance of type I and type II traps. We thus hypothesized that in the Rb_3InCl_6:xSb^{3+} (Δ = 1.5%) sample the broad and continuous trap distribution could compensate losses from the STE center at the various temperatures probed, and thus offered the maximum value of T_c. Overall, these data support the hypothesis that a non-stoichiometric amount of In^{3+} in the synthesis introduced a high density of In vacancies, forming energy traps whose depth and distribution could be further regulated by varying Δ. With increasing temperature, non-radiative channels are progressively activated and lead to emission losses from STE, but such losses are compensated by the thermally activated energy transfer from trap states to STE. The whole process leads to a robust anti-TQ behavior.[2,6-9]

We also attempted to modify the structural rigidity, as this can enhance the anti-TQ behavior by suppressing the thermally-activated non-radiative relaxation channels, as it is well known in rare earth doped metal oxide/nitride phosphors.[6,17] We did this by alloying the Rb ions with either K^+ or Cs^+ in Rb_3InCl_6:xSb^{3+} while keeping fixed Δ at 1.5% and x at 1-2%. Alloying was corroborated by SEM-EDS analyses (Figure S20-21, Table S7) which revealed compositions corresponding to $Rb_{2.2}K_{0.8}InCl_6$ and $Cs_{0.7}Rb_{2.3}InCl_6$, respectively. The shrinking/expansion of the unit cell parameters upon alloying (according to XRD, see Figure S22) was not accompanied by the formation of impurity phases. For these two samples we then recorded the temperature dependent PL intensity in the 300-500 K range (Figure 2d and Figure S23) and used T_c to evaluate their anti-TQ behavior. The $Rb_{2.2}K_{0.8}InCl_6$:xSb^{3+} sample had a T_c of 450 K, lower than Rb_3InCl_6:xSb^{3+} (T_c=491 K). In contrast, the $Cs_{0.7}Rb_{2.3}InCl_6$.xSb^{3+} sample showed an enhanced T_c, as it had a PL intensity at 500 K (T_c>500 K) that corresponded to 110% of its initial RT value. This, to the best of our knowledge, this is the most robust anti-TQ behavior for a metal halide phosphor to date.[12,24]

We then recorded *in situ* temperature dependent XRD patterns for all the samples to evaluate their structural rigidity. As shown in Figure S24, for all samples, their diffraction peaks underwent reversible shifts during the heating-cooling cycle. In the Figure 2e, we plotted the temperature dependent 2ϴ position for each sample and evaluated their thermal expansion coefficients by comparing their slopes. For $Rb_{2.2}K_{0.8}InCl_6$, Rb_3InCl_6 and $Cs_{0.7}Rb_{2.3}InCl_6$, their fitted slopes were $-2.3*10^{-3}$ 2ϴ/K^{-1}, $-1.9*10^{-3}$ 2ϴ/K^{-1} and $-1.5*10^{-3}$ 2ϴ/K^{-1}, respectively, indicating a gradually enhanced structural rigidity. As shown in Figure S25, at higher temperature (423 K), the Raman peaks of the $K_xRb_{3-x}InCl_6$:xSb^{3+} shifted to lower frequencies. This is ascribed to a volume effect stemming from the thermal expansion of the octahedra. In contrast, the peak of the Rb_3InCl_6:xSb^{3+} sample at 423 K was essentially at the same spectral position as the one at 300 K, indicating negligible variation in the stretching mode. Such comparison indicated a higher rigidity of the $[InCl_6]^{3-}$ octahedra in Rb_3InCl_6:xSb^{3+} lattice than in the $K_xRb_{3-x}InCl_6$: xSb^{3+}. Considering also a higher T_c of Rb_3InCl_6:xSb^{3+}, we can ascribe the better anti-TQ behavior of Rb_3InCl_6:xSb^{3+} to its higher rigidity. As it is well illustrated in metal oxide/nitride materials, a higher structural rigidity reduces the lattice expansion with increasing temperature and can suppress phonon-related non-radiative processes.[6,17] In our case, after alloying with Cs^+, the sample acquired higher structural rigidity, and this can explain the better anti-TQ behavior, while alloying with smaller K^+ cations results in a lower rigidity and worse anti-TQ behavior.[18] It is worth to note that the long-term stability of the Cs alloyed phosphor decreased compared with the non-alloyed one, as shown in Figure S26. To study whether the particle size has any influence on the anti-TQ behavior, we prepared three Rb_3InCl_6:xSb^{3+} samples with different average particle sizes. One sample corresponded to the powder Rb_3InCl_6:xSb^{3+} with a domain size of 62 nm as delivered from the synthesis. The other two were obtained from it by grinding it for 5 and 15 minutes, respectively, in order to progressively reduce the average domain size to 29 nm and to 19 nm, respectively. This process ensures that the two "secondary" samples have the same chemical composition as the primary sample. As shown in Figure S27a-d, XRD and SEM analyses confirm a progressive reduction in average particle size with grinding, however this size variation has no influence on the anti-TQ behavior, as shown in Figure S27e-f.

Based on the control experiments, a model of the anti-TQ behavior of the A_3InCl_6 phosphor can be drawn, as shown in Figure 2f. After light excitation (3.3 eV), the Sb dopant ($^1S_0 \rightarrow {}^3P_1$) is firstly sensitized (**1**). The generated exciton is heavily confined within a $[SbCl_6]^{3-}$ octahedron and interacts with the crystal lattice, which results in enhanced electron–phonon coupling and formation of a self-trapped exciton (**2**). Most trapped excitons decay radiatively to the ground state and generate green emission (**3**), while a fraction of them couple with lattice phonons more strongly and decay non-radiatively with a faster kinetics[35] (**4**). With increasing temperature, the lattice vibrations are enhanced and accelerate fast non-radiative processes (**4**), which result in emission loss of the phosphor. Here the materials with higher structural rigidity tend to have higher-energy phonon modes, which decreases the probability of non-radiative relaxation[36] (**4**). On the other hand, the energy transfer from trap states to STE is also thermally activated

(**5**) and can compensate the emission losses (**4**) at increasing temperature. In process (**5**), a broad and deep trap distribution is required to compensate the non-radiative emission loss at each heating stage, which can be realized by tuning the stoichiometric deficiency (Δ) of the In precursors in the synthesis.

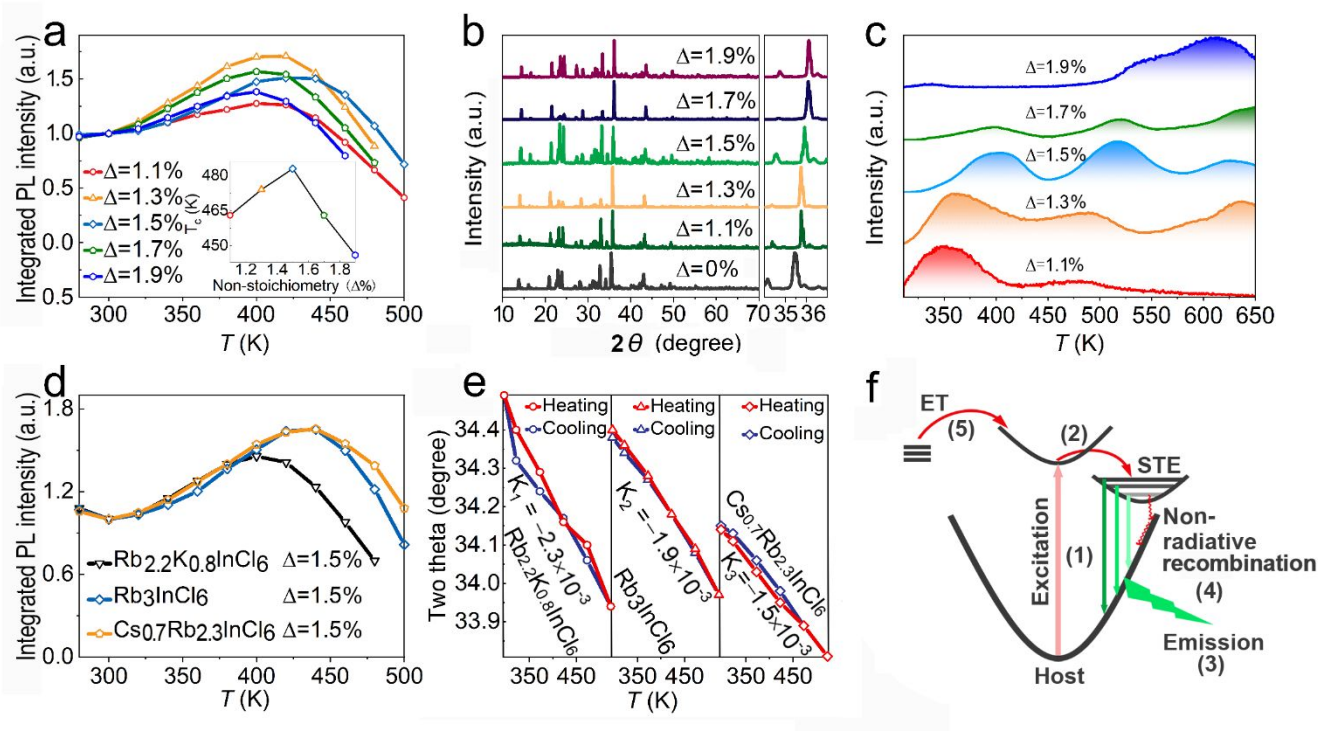

Figure 2. (a) PL intensity of Rb_3InCl_6:xSb^{3+} with different values of the stoichiometric deficiency of In (Δ = 0%, 1.1%, 1.3%, 1.5%) in the temperature range from 300 K to 500 K. The PL intensity was normalized to the intensity recorded at 300 K. (b) XRD spectra of Rb_3InCl_6:xSb^{3+} with different Δ values. The right panel shows a zoom of the pattern in the range of 35-37 degrees. (c) Thermoluminescence spectra of the Rb_3InCl_6:xSb^{3+} with different Δ values; (d) PL intensity of $Rb_{2.2}K_{0.8}InCl_6$:xSb^{3+}, Rb_3InCl_6:xSb^{3+} and $Cs_{0.7}Rb_{2.3}InCl_6$:xSb^{3+} in the temperature range from 300 K to 500 K. The PL intensity was normalized to the intensity at 300 K; (e) 2Θ position of diffraction peaks in the temperature range from 300-500 K and their fitted slope. All the data are extracted from the temperature dependent XRD patterns in the heating-cooling cycle. (f) Scheme of emission process of anti-TQ metal halide phosphor along heating under UV light excitation.

The high rigid metal oxide/nitride materials experience only negligible lattice expansion with increasing temperature and thus maintain robust anti-TQ behavior,[37] while the metal halides experience more significant thermal expansion under the same conditions (Figure 2e). To understand how the Rb_3InCl_6:xSb^{3+} maintain stable luminescence under lattice expansion, we performed a Rietveld refinement of the XRD patterns and carried out Raman spectroscopy to investigate the structural changes taking place under heating. A sample of 3D metal halide ($Cs_2AgInCl_6$:xSb^{3+}) powders was prepared and underwent the same analyses for comparison. This sample has the same emissive center ($[SbCl_6]^{3-}$) as Rb_3InCl_6:xSb^{3+}, but a different connectivity of the octahedra (3D vs 0D).[35] In particular, we wanted to elucidate whether the connectivity had any substantial influence on the temperature-dependent structural changes and luminescence. The doping concentration of Sb^{3+} was determined as 1.2% in the $Cs_2AgInCl_6$:xSb^{3+} sample, similar to Rb_3InCl_6:xSb^{3+} (Figure S28 and Table S8-9). Temperature dependent PL spectra of $Cs_2AgInCl_6$:xSb^{3+} indicated a significant decline in PL intensity with increasing temperature in the range from 298 K to 420 K (Figure S29). We could exclude the possibility that the PL quenching was caused by the structural deterioration caused by heating, as the temperature dependent XRD patterns always showed pure 3D double perovskite phase, with reversible shift of diffraction peaks across the heating-cooling cycle (Figure 3a). Hence the 3D $Cs_2AgInCl_6$:x% Sb^{3+} was also structurally stable at various temperatures, similarly to the 0D Rb_3InCl_6:xSb^{3+} sample. We have estimated the temperature dependent lifetime for the anti-TQ phosphors Rb_3InCl_6:xSb^{3+} and the TQ phosphor $Cs_2AgInCl_6$:xSb^{3+} as control sample. The data are reported in Tables S10-11 and Figure S30. Both phosphors evidence a shortening of the PL lifetime with increasing temperature. For the 3D $Cs_2AgInCl_6$:xSb^{3+} phosphor, the lifetime at 400K is about 3.4 times shorter than the one at 300K (τ_{300K}/τ_{400K} = 3.4). In the same temperature range, the lifetime of the 0D Rb_3InCl_6:xSb^{3+} sample shows a more modest shortening (τ_{300K}/τ_{400K} = 1.2). These results indicate that the $[SbCl_6]^{3-}$ is surrounded by a relatively more stable environment in the 0D framework compared to the 3D framework in the temperature range probed in this work. Overall, the 0D sample showed more robust luminescence stability at increasing temperature than the 3D one.

We then carried out Rietveld refinement on the XRD spectra of the 0D and 3D samples at 300 K, 425 K and 525 K, respectively (Figure S31-32, Table S12). As the doping concentrations of Sb^{3+} for both cases were very low (~1%), we treated Sb^{3+} and In^{3+} equally as B^{3+} in the refinement. The temperature dependent A-Cl and B-Cl bond lengths were plotted for the 3D sample (Figure 3b) and the 0D sample (Figure 3c), respectively. In particular, the variation of the A-Cl bond length represents a variation in the distance between two octahedra, while the variation of the B-Cl bond length represents the expansion of an individual octahedron. For the 3D case (Figure 3b), both the A-Cl and B-Cl lengths show linear elongation with increasing temperature, indicating a synchronized stretching of the individual octahedra and of the distance between the connected octahedra. In contrast, for the 0D case (Figure 3c), the A-Cl length increased linearly with temperature from 300 K to 525 K, while the B-Cl length remained unchanged. Quantitively, with temperature increasing from 300 K to 500 K, the cell was slightly distorted (0.3% tilt of □), and the cell volume expanded by about 3%. In contrast, the Sb-Cl bond length (in this work, we treated Sb^{3+} and In^{3+} equally as B^{3+} in the refinement) varies varied little with temperature (it shrinks by 0.4%). Such results indicate that the overall geometry of the $[SbCl_6]^{3-}$ octahedron in Rb_3InCl_6:xSb^{3+} does not change much with temperature, a behavior that we ascribe to the 0D structure of this material, formed by isolated octahedra. We carried molecular dynamic (MD) simulations to model the temperature dependent structural evolution of $[InCl_6]^{3-}$ octahedra. The results are consistent with the XRD Rietveld refinement, indicating that the lattice volume expands gradually from 300K to 500K. The dilation of the lattice mainly led to an increase of the In-In distance from 7.52 Å at 300K to 7.56 Å at 400K and 7.58 Å at 500K, while the octahedra remained almost unaffected at the different temperatures. Specifically, In-Cl bond lengths and Cl-In-Cl bond angles were not affected by the temperature: the In-Cl bond lengths remained fixed at 2.55 Å from 300K to 500 K and the bond angles also stayed fixed at around 90° in the same temperature range. These results indicate that the $[BCl_6]^{3-}$ octahedra were not much affected by temperature and the main contribution in the thermal expansion of the lattice in the 0D sample was essentially an increase in the distance between the octahedra.

The different expansion behaviors of the 0D and 3D sample were further verified by temperature-dependent Raman spectra. As shown in Figure 3d and 3e, the Raman spectra of $Cs_2AgInCl_6$:xSb^{3+} and Rb_3InCl_6:xSb^{3+} evidenced similar profiles, with the two peaks at 175 cm^{-1} and 300 cm^{-1} corresponding to the symmetric vibration stretching of the $[InCl_6]^{3-}$ octahedron.[38] At higher temperature (425 K), the Raman peaks of the 3D sample shifted to lower frequencies. Such change can be ascribed to a volume effect stemming from the thermal expansion of the octahedron.[39] In contrast, the peak of the 0D sample at 425 K was essentially at the same spectral position as the one at 300 K, indicating that the stretching mode of isolated octahedra varied little with temperature.

We have employed deformation potential (DP) theory to evaluate the electron-phonon (e-p) interactions of the 0D Rb_3InCl_6, 3D $Cs_2AgInCl_6$ and the reported anti-TQ metal oxide $CaScAlSiO_6$.[40] The DP theory considers the interaction with acoustic phonons as the main scattering mechanism for the electrons. It has been successfully applied to the study of materials such as metal coordination polymers,[41] organic polymers,[42] and perovskites[43] for the description of the electron-phonon interaction strength. The electron-phonon interaction matrix is described as $|M(k,k')|^2 = k_B T E_1^2/C_{ii}$. Here E_1 is the DP constant and C_{ii} is the elastic constant, k and k' electron states. Therefore, a large E_1 and small C_{ij} will indicate stronger electron-phonon (e-p) interactions and *vice versa*. The 0D Rb_3InCl_6, 3D $Cs_2AgInCl_6$ and $CaScAlSiO_6$ structures have similar C_{ij} values. However, the E_1 value of 0D (10.62) is much smaller than those of both the 3D $Cs_2AgInCl_6$ (21.93) and of $CaScAlSiO_6$ (22.31). Therefore, the 0D structure has weaker electron-phonon interactions than both the 3D $Cs_2AgInCl_6$ and $CaScAlSiO_6$. To reveal how the surrounding environment of $[SbCl_6]^{3-}$ changes with increasing temperature, we carried out temperature dependent PLE experiments and DFT calculations on 0D Rb_3InCl_6:xSb^{3+}. As shown in Figure S34a, the PLE peaks position of the Rb_3InCl_6:xSb^{3+} sample is temperature independent, indicating almost no variation in the environment surrounding the $[SbCl_6]^{3-}$ octahedra in Rb_3InCl_6:xSb^{3+} (in the 300-500 K temperature range). The temperature dependent PLE spectra of the 3D $Cs_2AgInCl_6$:xSb^{3+} sample have also been collected (Figure S34b). The spectra evidence a progressive decrease in the intensity of the peak at 370 nm with increasing temperature, from 300 to 500K. Such result indicates more drastic changes in the local environment of the $[SbCl_6]^{3-}$ octahedra in 3D $Cs_2AgInCl_6$:xSb^{3+}. The DFT results again support a temperature independent local structure of $[SbCl_6]^{3-}$ in the 0D Rb_3InCl_6:xSb^{3+} lattice in the 300-500 K range. We have computed the density of states (DOS) of 0D Rb_3InCl_6:xSb^{3+} at 300 K, 400 K, 500 K. The high temperature structures were obtained using molecular dynamics simulations. The DOS profile stays essentially the same at the different temperatures probed, with calculated band gap values likewise remaining almost unchanged (2.71 eV at 300 K, 2.71 eV at 400 K and 2.68 eV at 500 K, respectively).

Overall, the structural evolution of the 3D $Cs_2AgInCl_6$:xSb^{3+} and 0D Rb_3InCl_6:xSb^{3+} can be represented in the sketch of Figure 3f-g. For the 3D structure, as the octahedra are connected in all x-y-z directions, each octahedron has to stretch following the thermal expansion of the whole structure. For the 0D structure, the isolated octahedra are decoupled from the rest of the structure. With increasing temperature, the distance between the octahedra increases to contribute to the thermal expansion of the structure, while the single octahedra do not expand much. As a result, the isolated octahedra (also the emissive centers) in the 0D structure exhibit higher rigidity with increasing temperature than the connected octahedra in the 3D structure. We propose that the intrinsic rigidity of the octahedra in 0D Rb_3InCl_6:xSb^{3+} can be one of the reasons for its robust anti-TQ properties. Further exploration on other 0D metal halides sample as anti-TQ phosphors are ongoing.

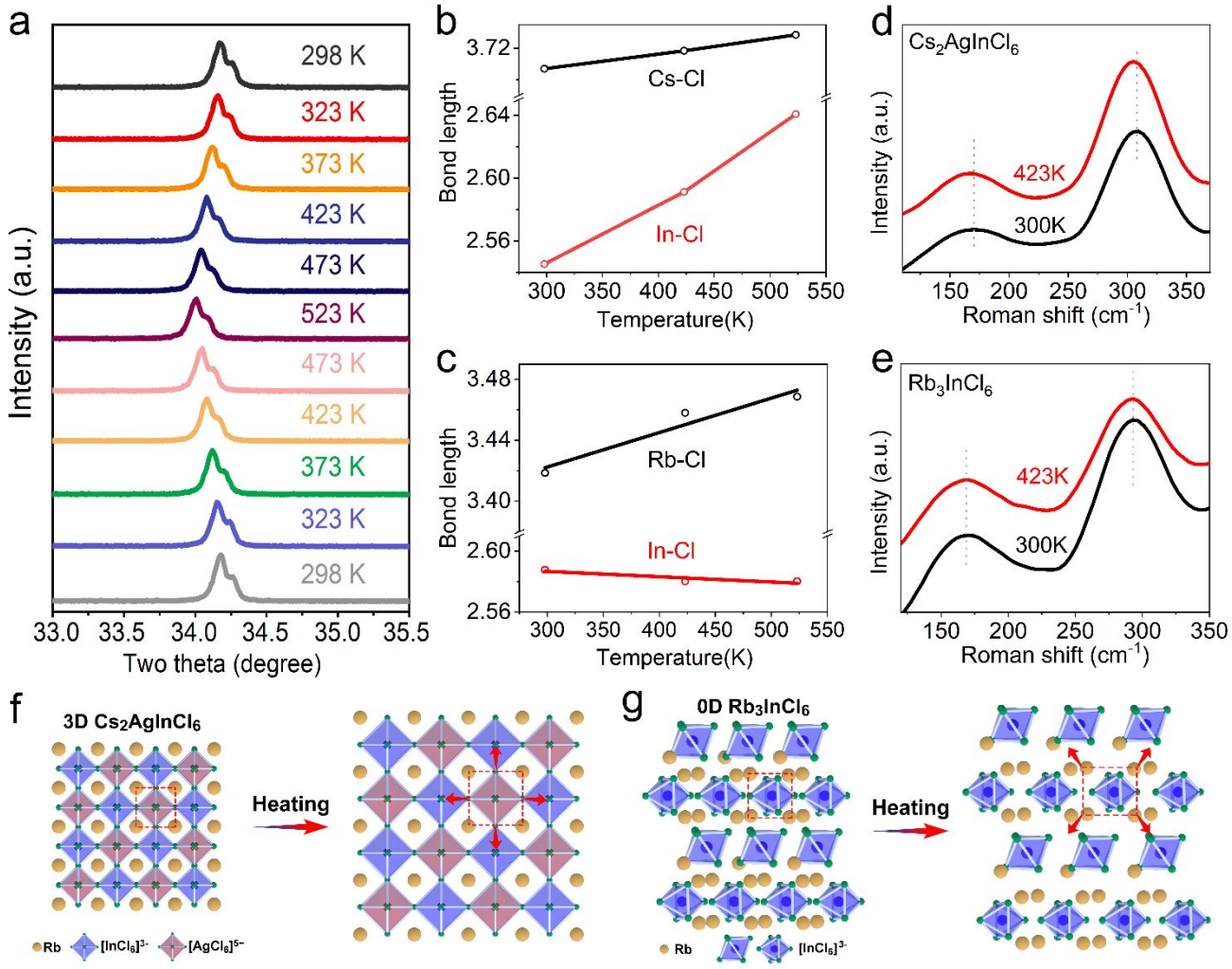

Figure 3. (a) Temperature dependent XRD spectra of $Cs_2AgInCl_6$:xSb^{3+} in the temperature range from 298 K to 523 K. (b-c) A-Cl and B-Cl bond length variation of at different temperatures (298 K to 523 K) for (b) $Cs_2AgInCl_6$:xSb^{3+} and (c) Rb_3InCl_6:xSb^{3+}, obtained by Rietveld refinement of XRD data. Temperature dependent Raman spectra of (d) $Cs_2AgInCl_6$:xSb^{3+} and (e) Rb_3InCl_6:xSb^{3+}. (f-g) Sketch of the structural expansion with increasing temperature of $Cs_2AgInCl_6$:xSb^{3+} and Rb_3InCl_6:xSb^{3+}.

Fabrication and testing of the hp-WLED devices. We then assessed the practical feasibility of the Rb_3InCl_6:xSb^{3+} phosphor by fabricating a hp-WLED using a blue LED chip as a light source (λ_{max}=380 nm). The result is shown in Figure 4. In general, high-power LED lighting requires high flux operating currents in the range 200-1000 mA. The commercial green phosphor, rare earth doped metal oxide $(Sr,Ba)_2SiO_2$:Eu was used as control sample, with a emission peak at 525 nm. We first coated the Rb_3InCl_6:xSb^{3+} or $(Sr,Ba)_2SiO_2$:Eu solely on the blue LED chip, respectively. As shown in Figure 4a, the luminescence intensity of both Rb_3InCl_6:xSb^{3+} and $(Sr,Ba)_2SiO_2$:Eu was enhanced with increasing current in the low current range (200-600 mA). However, in the higher current range (600-2000 mA), the luminescence intensity of the commercial $(Sr,Ba)_2SiO_2$:Eu sample started to decline, while the Rb_3InCl_6:xSb^{3+} sample delivered an increasing intensity, showing a parallel trend with the blue LED chip. We then assembled the blue LED chip, green phosphor (either Rb_3InCl_6:xSb^{3+} or $(Sr,Ba)_2SiO_2$:Eu) and the red emissive commercial anti-TQ phosphor K_2SiF_6:Mn^{4+} (KSF) in a WLED package (Figure 4b-f). As show in Figure 4c, the overall luminescence intensity of $(Sr,Ba)_2SiO_2$:Eu based WLED started to decrease when the applied current was over 600 mA. In contrast, the Rb_3InCl_6:xSb^{3+} based WLED preserved enhanced luminescence at increasing currents up to 1600 mA and maintained its intensity up to 2000 mA (Figure 4b and 4c), corresponding to an operation temperature of ~500 K (Figure S36). We also compared the color coordinates stability of the two types of WLED. As show in Figure 4d, the Rb_3InCl_6:xSb^{3+} based WLED sustained its white color well in the 200-2000 mA current range. The color rendering index (CRI) value of the WLED at a current of 2000 mA was equal to 101% of the initial CRI at 200 mA, with a luminous flux of ~21 lm (Table S13), comparable with the well-known metal oxide based anti-TQ phosphor[2]: NSPO:0.03Eu^{2+}. In contrast, the $(Sr,Ba)_2SiO_2$:Eu based WLED changed its color from white to red gradually, because the red emissive KSF showed anti-TQ behavior, while the green emissive $(Sr,Ba)_2SiO_2$:Eu was gradually quenched at higher currents. The corresponding operated WLED at 200 mA and 2000 mA was shown in Figure 4e (Rb_3InCl_6:xSb^{3+} based) and 4f ($(Sr,Ba)_2SiO_2$:Eu), respectively. The fabricated Rb_3InCl_6:xSb^{3+}-based WLED (Figure 4e) exhibited stable bright white emission at high applied current, showing excellent color stability. The aging experiments show that the Rb_3InCl_6:xSb^{3+} based devices exhibit long-term stability against humidity and large current, as reported in Figures S37-39. These results demonstrate that Rb_3InCl_6:xSb^{3+} is a

robust anti-TQ phosphor that can be successfully used as a green-emitting phosphor in high-power WLED lighting.

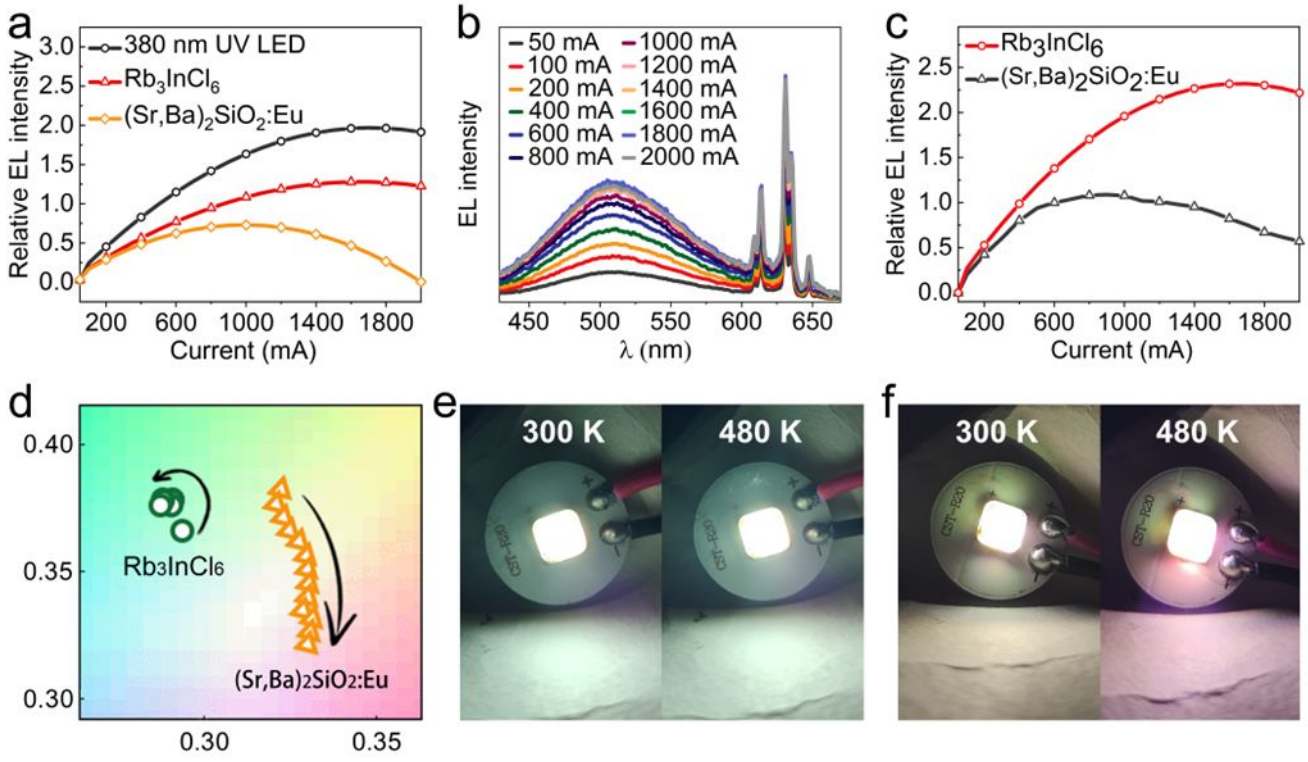

Figure 4. Performance of the fabricated pc-LEDs under high flux operating current. (a) Electroluminescensce (EL) spectra of Rb_3InCl_6:xSb^{3+} (red line and triangle) and the commercial green phosphor $(Sr,Ba)_2SiO_2$:Eu (orange line and diamond) coated on the blue LED chip under a high flux operating current of 100–2000 mA. The EL intensity of blue LED was also recorded for reference (black line and circle). (b) EL spectra of WLED using Rb_3InCl_6:xSb^{3+} as green phosphor and KSF as the red component under the current range from 50 mA to 2000 mA. (c) EL intensity of the WLED using Rb_3InCl_6:xSb^{3+} as the green component and KSF as red phosphor (red line and circle) and the WLED using commercial $(Sr,Ba)_2SiO_2$:Eu as green phosphor and KSF as red phosphor (black line and triangle), under the current range of 50 mA to 2000 mA. (d) CIE chromaticity coordinates of the Rb_3InCl_6:xSb^{3+} prototype WLED compared to the commercial green rare-earth oxide phosphor-based WLED, under increasing current (from 50 mA to 2000 mA). (e) Photographs of the Rb_3InCl_6:xSb^{3+} WLED prototype at low current (left) and high current (right). (f) Photographs of the fabricated $(Sr,Ba)_2SiO_2$:Eu WLED prototype at low current (left) and high current (right).

Conclusion

In summary, we have successfully developed a non-toxic and rare-earth-free metal halide phosphor, $A_3In_{1-\Delta}Cl_6$:xSb^{3+} that does not suffer from luminescence TQ up to 500 K, achieving by non-stoichiometric synthesis and A site alloying. This behavior is attributed to the compensation of emission losses by the energy transfer from the induced defects to STE. At the same time, the intrinsic structural rigidity of the octahedra in the 0D metal halides reduces the thermal activated non-radiative energy losses. The nontoxic nature of the material, its low temperature synthesis and high QY make A_3InCl_6:xSb^{3+} an ideal anti-TQ phosphor for high-power WLED, with stable bright emission at an applied current of 2000 mA, corresponding to a working temperature of ~500 K. We want to remark that the class of metal halide materials is vast. Hence there are many members of this class (some of them even yet to be discovered) which have, or could have, high PLQY with emission ranging from the blue to NIR region. Our work indicates that, with proper design, the emitting center of metal halides with a "soft lattice" provided by the 0D structure could have the proper intrinsic rigidity to exhibit an anti-TQ behavior as robust as the one of mainstream metal oxide/nitrides. On the light of these considerations, the various reported Sb doped phosphors and other zero-dimensional metal halide materials could, in principle, be good anti-TQ phosphors, however only after proper optimization following the principles and guidelines mentioned above. We believe that our work will inspire the community to identify additional viable, robust, broadband emitting anti-TQ phosphors within the large family of metal halides.

ASSOCIATED CONTENT

Supporting Information.
This material is available free of charge and include the below parts:
Experimental part and Table S1: synthesis details and characterization method; S1-S3: PLQY, temperature dependent PL and cooling/heating cycle; S4-S14, S20-S24, S27 and Table

S2-S9: structure/morphology/composition characterization; S15-S17: PL stability test; S18-S19: Defects characterization; S28-S35: Comparison of anti-TQ behavior between3D and 0D sample; S24, S36-S38 and Table S13: performance of hp-WLED device.

AUTHOR INFORMATION

Corresponding Authors

liberato.manna@iit.it

sylu2013@zzu.edu.cn

Author Contributions

Yi Ru$^{\triangledown}$ and Baowei Zhang$^{\triangledown}$ contributed equally to this work.

Notes

The authors declare no competing financial interest.

ACKNOWLEDGMENT

This work was supported by the National Natural Science Foundation of China (Nos. 22305224, Nos. 52122308 and 51973200), the China Postdoctoral Science Foundation (2022TQ0290) and the Ministry of Science and Technology of the People's Republic of China (DL2023026004L). X. Y. would like to thank the support from Leverhulme Trust. We thank the Center of Advanced Analysis & Gene Sequencing, Zhengzhou University, for SEM, and ICP test.

REFERENCE

(1) Ożadowicz, A.; Grela, J. Energy saving in the street lighting control system—a new approach based on the EN-15232 standard. *Energy Efficiency* **2017,** *10* (3), 563.

(2) Kim, Y. H.; Arunkumar, P.; Kim, B. Y.; Unithrattil, S.; Kim, E.; Moon, S.-H.; Hyun, J. Y.; Kim, K. H.; Lee, D.; Lee, J.-S.et al. A zero-thermal-quenching phosphor. *Nature Materials* **2017,** *16* (5), 543.

(3) Guo, F.; Yuan, R.; Yang, Y.-L.; Zhao, J.-T.; Lin, H.; Zhang, Z.-J. An effective heat dissipation strategy improving efficiency and thermal stability of phosphor-in-glass for high-power WLEDs. *Ceramics International* **2022,** *48* (9), 13185.

(4) Amachraa, M.; Wang, Z.; Chen, C.; Hariyani, S.; Tang, H.; Brgoch, J.; Ong, S. P. Predicting Thermal Quenching in Inorganic Phosphors. *Chemistry of Materials* **2020,** *32* (14), 6256.

(5) Munoz, G.; De La Cruz, C.; Munoz, A.; Rubio, J. High-temperature luminescence properties of Eu^{2+}-activated alkali halide phosphor materials. *Journal of materials science letters* **1988,** *7*, 1310.

(6) Zhao, M.; Xia, Z.; Huang, X.; Ning, L.; Gautier, R.; Molokeev, M. S.; Zhou, Y.; Chuang, Y.-C.; Zhang, Q.; Liu, Q.et al. Li substituent tuning of LED phosphors with enhanced efficiency, tunable photoluminescence, and improved thermal stability. *Science Advances* **2019,** *5* (1), eaav0363.

(7) Dang, P.; Wang, W.; Lian, H.; Li, G.; Lin, J. How to Obtain Anti-Thermal-Quenching Inorganic Luminescent Materials for Light-Emitting Diode Applications. *Advanced Optical Materials* **2022,** *10* (6), 2102287.

(8) Zhang, Q.; He, M.; Wan, Q.; Zheng, W.; Liu, M.; Zhang, C.; Liao, X.; Zhan, W.; Kong, L.; Guo, X.et al. Suppressing thermal quenching of lead halide perovskite nanocrystals by constructing a wide-bandgap surface layer for achieving thermally stable white light-emitting diodes. *Chemical Science* **2022,** *13* (13), 3719.

(9) Qiao, J.; Ning, L.; Molokeev, M. S.; Chuang, Y.-C.; Liu, Q.; Xia, Z. Eu2+ Site Preferences in the Mixed Cation $K_2BaCa(PO_4)_2$ and Thermally Stable Luminescence. *Journal of the American Chemical Society* **2018,** *140* (30), 9730.

(10) Liu, M.; Wan, Q.; Wang, H.; Carulli, F.; Sun, X.; Zheng, W.; Kong, L.; Zhang, Q.; Zhang, C.; Zhang, Q.et al. Suppression of temperature quenching in perovskite nanocrystals for efficient and thermally stable light-emitting diodes. *Nature Photonics* **2021,** *15* (5), 379.

(11) Huang, G.; Wang, C.; Xu, S.; Zong, S.; Lu, J.; Wang, Z.; Lu, C.; Cui, Y. Postsynthetic Doping of $MnCl_2$ Molecules into Preformed $CsPbBr_3$ Perovskite Nanocrystals via a Halide Exchange-Driven Cation Exchange. *Advanced Materials* **2017,** *29* (29), 1700095.

(12) Zhou, X.; Han, K.; Wang, Y.; Jin, J.; Jiang, S.; Zhang, Q.; Xia, Z. Energy-Trapping Management in X-Ray Storage Phosphors for Flexible 3D Imaging. *Advanced Materials* **2023,** *35* (16), 2212022.

(13) Lin, C. C.; Tsai, Y.-T.; Johnston, H. E.; Fang, M.-H.; Yu, F.; Zhou, W.; Whitfield, P.; Li, Y.; Wang, J.; Liu, R.-S.et al. Enhanced Photoluminescence Emission and Thermal Stability from Introduced Cation Disorder in Phosphors. *Journal of the American Chemical Society* **2017,** *139* (34), 11766.

(14) Wang, L.; Xie, R.-J.; Suehiro, T.; Takeda, T.; Hirosaki, N. Down-Conversion Nitride Materials for Solid State Lighting: Recent Advances and Perspectives. *Chemical Reviews* **2018,** *118* (4), 1951.

(15) Fang, M.-H.; Mariano, C. O. M.; Chen, K.-C.; Lin, J.-C.; Bao, Z.; Mahlik, S.; Lesniewski, T.; Lu, K.-M.; Lu, Y.-R.; Wu, Y.-J.et al. High-Performance $NaK_2Li[Li_3SiO_4]_4$:Eu Green Phosphor for Backlighting Light-Emitting Diodes. *Chemistry of Materials* **2021,** *33* (5), 1893.

(16) Yang, Z.; de Boer, T.; Braun, P. M.; Su, B.; Zhang, Q.; Moewes, A.; Xia, Z. Thermally stable red‐emitting oxide ceramics for laser lighting. *Advanced Materials* **2023**, 2301837.

(17) Yang, Z.; de Boer, T.; Braun, P. M.; Su, B.; Zhang, Q.; Moewes, A.; Xia, Z. Thermally Stable Red-Emitting Oxide Ceramics for Laser Lighting. *Advanced Materials* **2023,** *35* (30), 2301837.

(18) Viswanath, N. S. M.; Krishnamurthy Grandhi, G.; Tran Huu, H.; Choi, H.; Jun Kim, H.; Min Kim, S.; You Kim, H.; Park, C.-J.; Bin Im, W. Zero-thermal-quenching and improved chemical stability of a UCr_4C_4-type phosphor via crystal site engineering. *Chemical Engineering Journal* **2021,** *420*, 127664.

(19) Ma, X.; Wang, Y. Local Structure and Self-Defect Evolution under Nonstoichiometric Effect Unlock Zero-Thermal-Quenching. *Advanced Optical Materials* **2023,** *11* (7), 2202765.

(20) Tang, Z.; Liu, R.; Chen, J.; Zheng, D.; Zhou, P.; Liu, S.; Bai, T.; Zheng, K.; Han, K.; Yang, B. Highly Efficient and Ultralong Afterglow Emission with Anti-Thermal Quenching from $CsCdCl_3$: Mn Perovskite Single Crystals. *Angewandte Chemie International Edition* **2022,** *61* (51), e202210975.

(21) Li, C.; Luo, Z.; Liu, Y.; Wei, Y.; He, X.; Chen, Z.; Zhang, L.; Chen, Y.; Wang, W.; Liu, Y.et al. Self-Trapped Exciton Emission with High Thermal Stability in Antimony-Doped Hybrid Manganese Chloride. *Advanced Optical Materials* **2022,** *10* (12), 2102746.

(22) Samanta, T.; Viswanath, N. S. M.; Jang, S. W.; Min, J. W.; Cho, H. B.; Han, J. H.; Im, W. B. Thermally Stable Self-Trapped Assisted Single-Component White Light from Lead-Free Zero-Dimensional Metal Halide Nanocrystals. *Advanced Optical Materials* **2023,** *11* (9), 2202744.

(23) Yuan, X.; Ji, S.; De Siena, M. C.; Fei, L.; Zhao, Z.; Wang, Y.; Li, H.; Zhao, J.; Gamelin, D. R. Photoluminescence Temperature Dependence, Dynamics, and Quantum Efficiencies in Mn^{2+}-Doped $CsPbCl_3$ Perovskite Nanocrystals with Varied Dopant Concentration. *Chemistry of Materials* **2017,** *29* (18), 8003.

(24) Han, J. H.; Viswanath, N. S. M.; Park, Y. M.; Cho, H. B.; Jang, S. W.; Min, J. W.; Im, W. B. Zero-Thermal-Quenching Layered Metal Halide Perovskite. *Chemistry of Materials* **2022,** *34* (12), 5690.

(25) Liu, Y.; Yan, S.; Wang, T.; He, Q.; Zhu, X.; Wang, C.; Liu, D.; Wang, T.; Xu, X.; Yu, X. Achieving Color-Tunable Long Persistent Luminescence in Cs_2CdCl_4 Ruddlesden-Popper Phase Perovskites. *Angewandte Chemie International Edition* **2023,** *62,* e202308420. doi.org/10.1002/anie.202308420

(26) Liu, S.; Fang, X.; Lu, B.; Yan, D. Wide range zero-thermal-quenching ultralong phosphorescence from zero-

dimensional metal halide hybrids. *Nature Communications* **2020,** *11* (1), 4649.

(27) Han, P.; Luo, C.; Yang, S.; Yang, Y.; Deng, W.; Han, K. All-Inorganic Lead-Free 0D Perovskites by a Doping Strategy to Achieve a PLQY Boost from <2 % to 90 %. *Angewandte Chemie International Edition* **2020,** *59* (31), 12709.

(28) Majher, J. D.; Gray, M. B.; Liu, T.; Holzapfel, N. P.; Woodward, P. M. Rb_3InCl_6: A Monoclinic Double Perovskite Derivative with Bright Sb^{3+}-Activated Photoluminescence. *Inorganic Chemistry* **2020,** *59* (19), 14478.

(29) Zhang, B.; Pinchetti, V.; Zito, J.; Ray, A.; Melcherts, A. E.; Ghini, M.; Pianetti, A.; Infante, I.; Brovelli, S.; De Trizio, L. Isolated $[SbCl_6]^{3-}$ Octahedra Are the Only Active Emitters in $Rb_7Sb_3Cl_{16}$ Nanocrystals. *ACS Energy Letters* **2021,** *6* (11), 3952.

(30) Dutzler, D.; Seibald, M.; Baumann, D.; Huppertz, H. Alkali Lithosilicates: Renaissance of a Reputable Substance Class with Surprising Luminescence Properties. *Angewandte Chemie International Edition* **2018,** *57* (41), 13676.

(31) Liu, Y.; Liu, G.; Wu, Y.; Cai, W.; Wang, Y.; Zhang, S.; Zeng, H.; Li, X. High-Temperature, Reversible and Robust Thermochromic Fluorescence Based on $Rb_2MnBr_4(H_2O)_2$ for Anti-Counterfeiting. *Advanced Materials* **2023,** *35,* 2301914.

(32) Karmakar, A.; Bernard, G. M.; Meldrum, A.; Oliynyk, A. O.; Michaelis, V. K. Tailorable Indirect to Direct Band-Gap Double Perovskites with Bright White-Light Emission: Decoding Chemical Structure Using Solid-State NMR. *Journal of the American Chemical Society* **2020,** *142* (24), 10780.

(33) Lätsch, L.; Kaul, C. J.; Yakimov, A. V.; Müller, I. B.; Hassan, A.; Perrone, B.; Aghazada, S.; Berkson, Z. J.; De Baerdemaeker, T.; Parvulescu, A.-N. et al. NMR Signatures and Electronic Structure of Ti Sites in Titanosilicalite-1 from Solid-State $^{47/49}$Ti NMR Spectroscopy. *Journal of the American Chemical Society* **2023,** *145* (28), 15018.

(34) Van den Eeckhout, K.; Smet, P. F.; Poelman, D. J. M. Persistent luminescence in Eu^{2+}-doped compounds: a review. **2010,** *3* (4), 2536.

(35) Zhu, D.; Zaffalon, M. L.; Zito, J.; Cova, F.; Meinardi, F.; De Trizio, L.; Infante, I.; Brovelli, S.; Manna, L. Sb-Doped Metal Halide Nanocrystals: A 0D versus 3D Comparison. *ACS Energy Letters* **2021,** *6* (6), 2283.

(36) Qiao, J.; Zhao, J.; Liu, Q.; Xia, Z. Recent advances in solid-state LED phosphors with thermally stable luminescence. *Journal of Rare Earths* **2019,** *37* (6), 565.

(37) Viswanath, N.; Grandhi, G. K.; Huu, H. T.; Choi, H.; Kim, H. J.; Kim, S. M.; Kim, H. Y.; Park, C.-J.; Im, W. B. Zero-thermal-quenching and improved chemical stability of a UCr_4C_4-type phosphor via crystal site engineering. *Chemical Engineering Journal* **2021,** *420*, 127664.

(38) Chen, F.; Wang, X.-J.; Bai, W.; Zhang, X.; Hao, W.; Zhang, C.; Xuan, T. Highly emissive Sb^{3+}-doped $Rb_2InCl_5{\cdot}H_2O$ perovskites: cost-effective synthesis, luminescence, and its application. *Journal of Materials Chemistry C* **2023,** *11* (32), 11010.

(39) Li, Z.; Wang, Y.; Jiang, J.; Liang, Y.; Zhong, B.; Zhang, H.; Yu, K.; Kan, G.; Zou, M. Temperature-dependent Raman spectroscopy studies of 1–5-layer WSe_2. *Nano Research* **2020,** *13* (2), 591.

(40) Liu, G.; Molokeev, M. S.; Xia, Z. J. C. o. M. Structural rigidity control toward Cr^{3+}-based broadband near-infrared luminescence with enhanced thermal stability. *Chemistry of Materials* **2022,** *34* (3), 1376.

(41) Yong, X.; Shi, W.; Wu, G.; Goh, S. S.; Bai, S.; Xu, J.-W.; Wang, J.-S.; Yang, S.-W. J. J. o. M. C. A. Tuning the thermoelectric performance of π–d conjugated nickel coordination polymers through metal–ligand frontier molecular orbital alignment. *Journal of Materials Chemistry A* **2018,** *6* (40), 19757.

(42) Yong, X.; Wu, G.; Shi, W.; Wong, Z. M.; Deng, T.; Zhu, Q.; Yang, X.; Wang, J.-S.; Xu, J.; Yang, S.-W. J. J. o. M. C. A. Theoretical search for high-performance thermoelectric donor–acceptor copolymers: the role of super-exchange couplings. *Journal of Materials Chemistry A* **2020,** *8* (41), 21852.

(43) Shi, W.; Yao, M.; Wu, X.; Zhou, T.; Yong, X.; Deng, T.; Ma, H.; Xi, J. J. A. S. Atomistic Insights into the Origin of High - Performance Thermoelectric Response in Hybrid Perovskites. *Advanced Science* **2023**, 2300666.

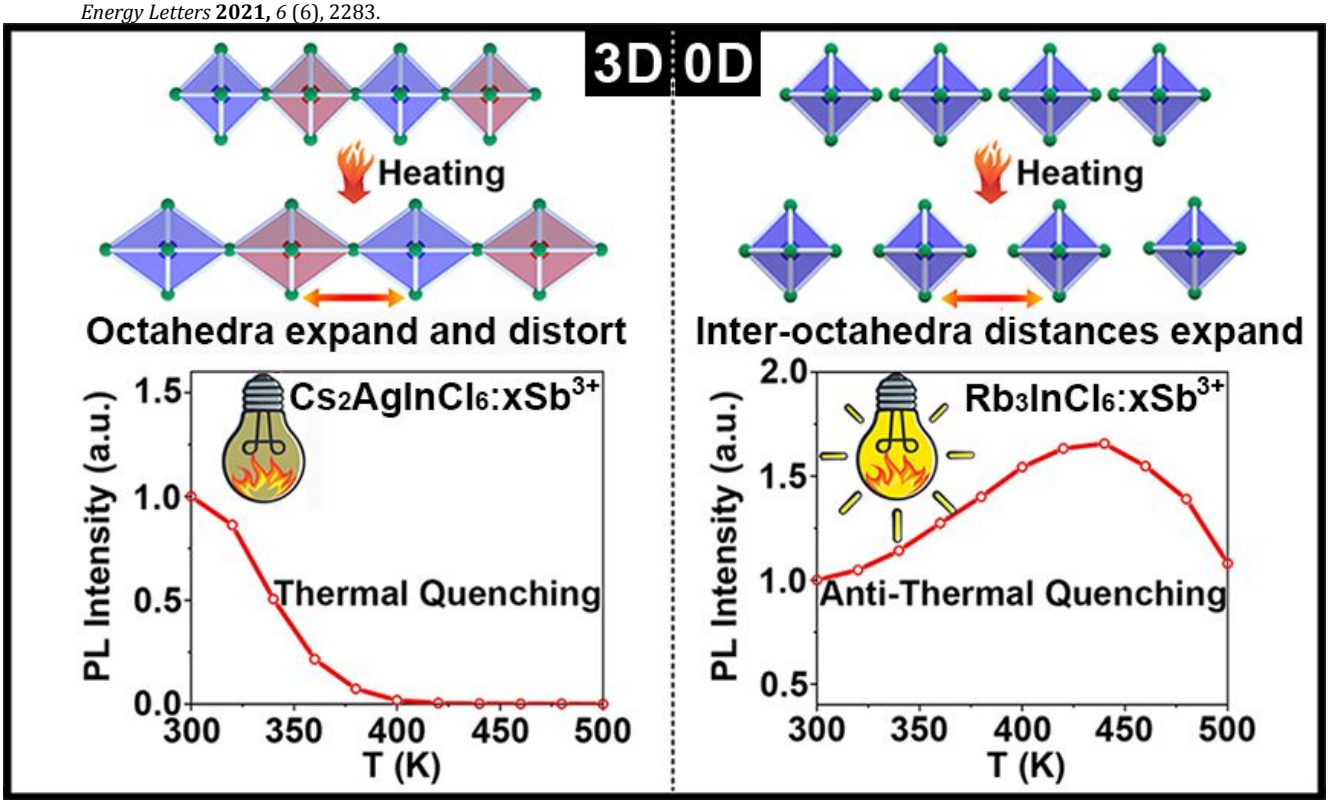

Table of Content